New results obtained from CALET observations after 8 years of data collection on the International Space Station

42nd International Conference on High Energy Physics

Sandro Gonzi[1,2,3] for the **CALET Collaboration**

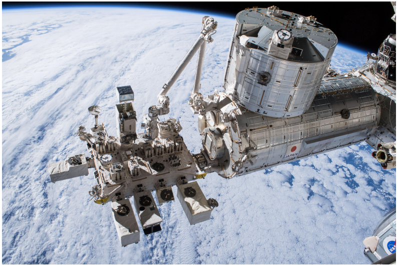

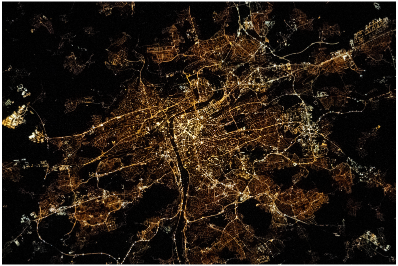

1. University of Florence, Department of Physics and Astronomy, Italy

2. National Institute for Nuclear Physics INFN, Division of Florence, Italy

3. National Research Council CNR, Institute of Applied Physics IFAC, Italy

The CALET mission

The **CALorimetric Electron Telescope (CALET)**, operating aboard the **International Space Station (ISS)** since October 2015, is an experiment dedicated to high-energy astroparticle physics.

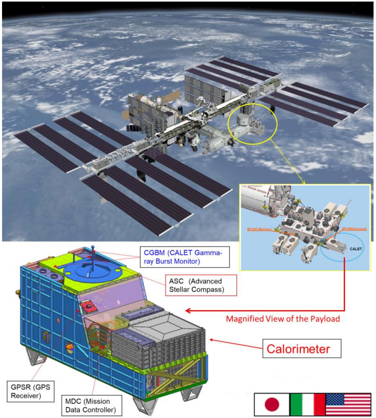

FIGURE 1: the CALET mission on the ISS.

Remarkable events:

- August 19th, 2015: launched by the Japanese H2-B rocket;
- August 25th, 2015: emplaced on JEM-EF (Japanese Experiment Module Exposed Facility) port #9;
- October 13th, 2015: start of stable observations, more than 4.5 billion events collected so far.

CALET payload

- **Mass** 612.8 kg (JEM Standard Payload)
- **Size**: 1850 mm(L) × 800 mm(W) × 1000 mm(H)
- **Power**: 507 W (max)
- **Telemetry**: Medium 600 kbps (6.5 GB/day)

The CALET payload

CALET consists of a **detector system and data processing units**, **support sensors** and an **interface unit** that attaches the payload to the JEM-EF.

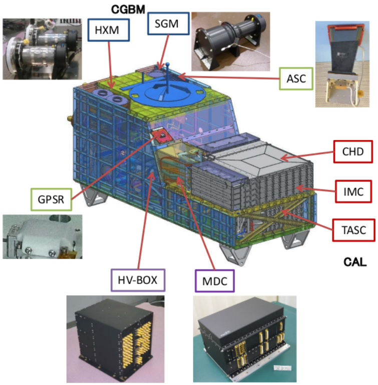

FIGURE 2: overview of the CALET payload.

Overview of the CALET payload:

- detector system:
  - main calorimeter (CAL):
    - CHarge Detector (CHD)
    - IMaging Calorimeter (IMC)
    - Total AbSorption Calorimeter (TASC)
  - CALET Gamma-ray Burst Monitor (CGBM):
    - Hard X-ray Monitor (HXM)
    - Soft Gamma-ray Monitor (SGM)
- data processing and power supply:
  - Mission Data Controller (MDC)
    CPU, telemetry, power, trigger, *etc.*
  - HV-BOX
    HV supply (PMT: 68ch, APD: 22ch)
- support sensors:
  - Advanced Stellar Compass (ASC)
    Directional measurement
  - GPS Receiver (GPSR)
    Time stamp of triggered event (< 1 ms)

CALET observations and physics targets

Overview of CALET observations:

- direct cosmic-ray observations in space at the highest energy region by combining:
  - √ a large-size detector;
  - √ long-term observation onboard the ISS;
- all electron observation in the 1 GeV - 20 TeV energy range, with high energy resolution;
  - ⇒ search for dark matter and nearby cosmic-ray sources;
- observation of cosmic-ray nuclei in the 10 GeV - 1 PeV energy range;
  - ⇒ unravelling the cosmic-ray acceleration and propagation mechanism;
- detection of transients in space by long-term stable observations:
  - ⇒ electromagnetic radiation from gravitational wave sources, gamma-ray bursts, solar flares, *etc.*

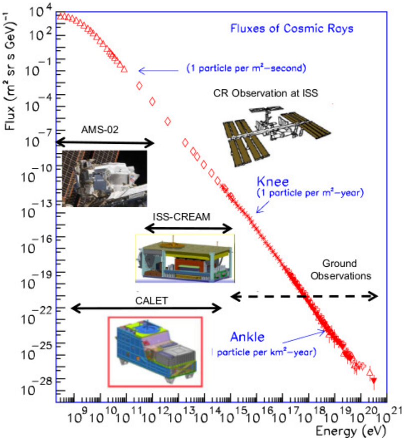

FIGURE 3: cosmic-ray observations on the ISS.

Experiments installed on the ISS

AMS-02 and CALET are carrying out complementary measurements.

The main detector (CAL)

The CALET main detector (CAL) [1] employs a **calorimeter** with a field of view of $\sim 45^\circ$ from zenith, a geometrical factor of $\sim 1040\ \mathrm{cm}^2$ sr and a total depth of $\sim$ **30 radiation length X_0** and $\sim$ **1.3 interaction length λ_I** for particles at normal incidence.

It consists of:

- **CHarge Detector (CHD)**: a pair of plastic scintillator hodoscopes arranged in two orthogonal layers, in order to identify the charge of the incident particle;
- **IMaging Calorimeter (IMC)**: a sampling calorimeter made of alternated thin layers of Tungsten absorber and scintillating fibers read-out individually;
- **Total AbSorption Calorimeter (TASC)**: a packed lead-tungstate (PWO) hodoscope, capable of almost complete containment of the TeV-electromagnetic showers.

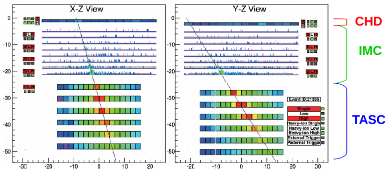

FIGURE 4: electron (or positron) event candidate (reconstructed energy of 3.05 TeV and energy deposit sum of 2.89 TeV).

This design leads to excellent **detector performance**: an electromagnetic shower energy resolution of $\sim 2\%$ above 20 GeV and a protons rejection factor of $\sim 10^5$.

[1] S. Torii, P. S. Marrocchesi *et al.*, *Adv. Space Res.*, **64** (2019) 2531

CALET operations in space

Three trigger modes are possible in CALET. The **High Energy (Low Energy) Trigger** select shower events with energies greater than 10 GeV (1 GeV), while the **Single Trigger** is dedicated to acquiring data from non-interacting particles for detector calibration.

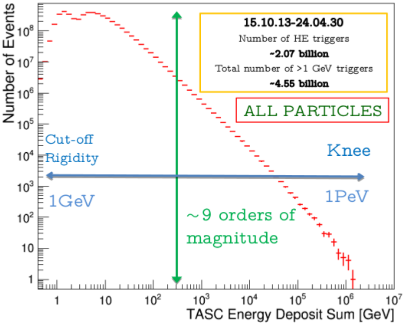

FIGURE 5: energy deposit (in TASC) spectrum in the range 1 GeV-1 PeV.

High energy (HE) trigger statistics:

- orbital operations: **3123 days (> 8 years)** as of April 30, 2024
- live time fraction: $\sim$ **86%**
- exposure of HE trigger: **> 275 m^2sr day**
- HE-gamma point source exposure: $\sim$ **4.2 m^2day** (for Crab, Geminga)

Geometrical Factor (GF)

- **GF = 1040 cm^2 sr** for electrons, light nuclei
- **GF = 1000 cm^2 sr** for gamma-rays
- **GF = 4000 cm^2 sr** for ultra-heavy nuclei

Time duration of observation: **20.6 hours per day** on average

All-electron spectrum

Spectrum measured [2] in
10.6 GeV $< E <$ 7.5 TeV

$$\Phi(E) = \frac{N(E)}{\Delta E\ \epsilon(E)\ S\Omega\ T}$$

$\Phi(E)$: electron spectrum
E: electron energy
$N(E)$: number of events in ΔE bin (after background subtraction)
$S\Omega$: geometrical acceptance (1040 cm^2 sr)
T: live time
ΔE: energy bin width
$\epsilon(E)$: total selection efficiency

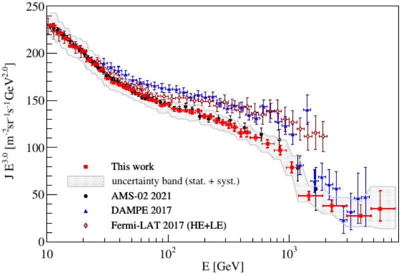

FIGURE 6: cosmic-ray all-electron spectrum measured by CALET compared with the results of AMS-02, DAMPE and Fermi-LAT.

Low energy region:

- the CALET spectrum is consistent with AMS-02 up to 2 TeV;
- present measurements are clustered below 1 TeV into 2 groups: **AMS-02 + CALET** and **Fermi-LAT + DAMPE**, possibly indicating the presence of unknown systematics.

High energy region:

- CALET observes a flux suppression above 1 TeV with a significance more than 6.5 σ.

[2] O. Adriani *et al.*, *Phys. Rev. Lett.* **131** (2023) 191001

Fit on the all-electron spectrum

Only nearby (< 1 kpc) and young (< 10^5 yr) sources can contribute to the flux above 1 TeV if the sources are supernova remnants (SNRs): a **steepening** at about 1 TeV is expected.

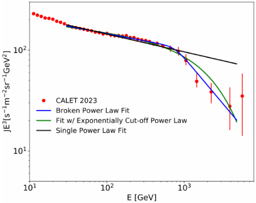

Figure 7a: fits in [30,4800] GeV.

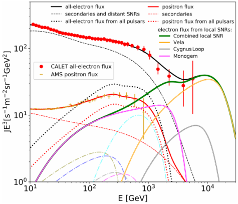

Figure 7b: possible spectral fit.

SBPL parameter	Fitted value	spectrum region
γ	-3.15 ± 0.01	low energy
$\Delta\gamma$	-0.77 ± 0.22	steepening
E_b	761 ± 115 GeV	steepening
s	0.1(*fixed*)	steepening
χ^2/dof	3.6/27	-

All-electron spectrum fitted in 30 GeV $< E <$ 4.8 TeV with a **single broken power law (SBPL)**:

$$\Phi(E) = C\left(\frac{E}{100\ \mathrm{GeV}}\right)^{\gamma}\left[1+\left(\frac{E}{E_b}\right)^{\frac{\Delta\gamma}{s}}\right]^{-s}$$

We observe that:

- in the TeV region the data show a break of the spectrum compatible with the DAMPE results;
- 9 candidates above 4.8 TeV are consistent with an estimation of the electron flux from the nearby SNRs based on an interpretation model.

Proton spectrum

Spectrum measured [3] in
50 GeV < E < 60 TeV

$$\Phi(E) = \frac{N(E)}{\Delta E\ \epsilon(E)\ S\Omega\ T}$$

$\Phi(E)$: proton spectrum
E: proton kinetic energy
$N(E)$: number of events in ΔE bin (after background subtraction)
$S\Omega$: geometrical acceptance (510 cm^2 sr)
T: live time
ΔE: energy bin width
$\epsilon(E)$: total selection efficiency

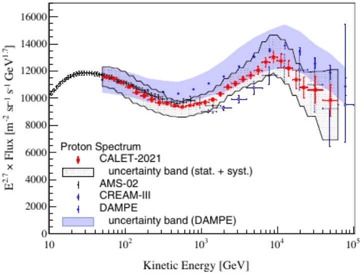

FIGURE 8: cosmic-ray proton spectrum measured by CALET compared with the experimental results of AMS-02, CREAM-III and DAMPE.

CALET spectrum is in good agreement with:

- rigidity spectra measured by magnetic spectrometers in the sub-TeV region;
- measurements carried out with calorimetric instruments at higher energies.

Observations

The analysis confirms the presence of a spectral **hardening** at a few hundred GeV (significance of more than 20 σ) and observes a spectral **softening** around 10 TeV.

[3] O. Adriani *et al.*, *Phys. Rev. Lett.* **129** (2022) 101102

Fit on the proton spectrum

ICHEP 2024

Proton spectrum is not consistent with a single power law covering the whole range.

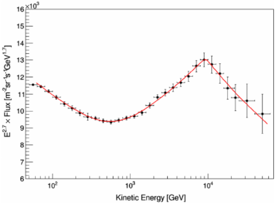

FIGURE 9A: fit with a DBPL function.

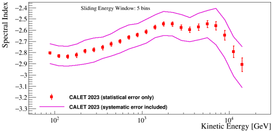

FIGURE 9B: spectral index vs. energy.

DBPL parameter	Fitted value	spectrum region
γ	$-2.83^{+0.01}_{-0.02}$	low energy
$\Delta\gamma$	$0.28^{+0.04}_{-0.02}$	hardening
E_0	584^{+61}_{-58} GeV	hardening
s	$2.4^{+0.8}_{-0.6}$	hardening
$\Delta\gamma_1$	$-0.34^{+0.06}_{-0.06}$	softening
E_1	$9.3^{+1.4}_{-1.1}$ TeV	softening
s_1	~ 30	softening
χ^2/dof	4.4/20	-

Proton spectrum fitted in $80\ \mathrm{GeV} < E < 60\ \mathrm{TeV}$ with a **double broken power law (DBPL)**:

$$\Phi(E) = C\left(\frac{E}{1\ GeV}\right)^{\gamma}\left[1+\left(\frac{E}{E_0}\right)^{s}\right]^{\frac{\Delta\gamma}{s}}\left[1+\left(\frac{E}{E_1}\right)^{s_1}\right]^{\frac{\Delta\gamma_1}{s_1}}$$

A gradual hardening is followed by a sharp softening at about 9 TeV ($s_1 >> s$, large uncertainty). Spectrum shape is consistent with the most recent results of DAMPE.

Helium spectrum

Spectrum measured [4] in
40 GeV < E < 250 TeV

$$\Phi(E) = \frac{N(E)}{\Delta E \, \epsilon(E) \, S\Omega \, T}$$

$\Phi(E)$: helium spectrum
E: helium kinetic energy
$N(E)$: number of events in ΔE bin (after background subtraction)
$S\Omega$: geometrical acceptance (510 cm^2 sr)
T: live time
ΔE: energy bin width
$\epsilon(E)$: total selection efficiency

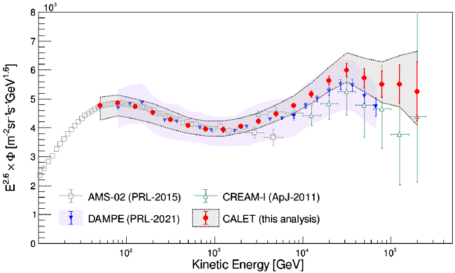

FIGURE 10: cosmic-ray helium spectrum measured by CALET compared with the experimental results of AMS-02, CREAM-I and DAMPE.

CALET spectrum is in good agreement with:

- rigidity spectra measured by magnetic spectrometers in the sub-TeV region;
- measurements carried out with calorimetric instruments at higher energies.

Observations

The analysis observes a spectral **hardening** from a few hundred GeV to a few tens TeV and also observes the onset of a spectral **softening** above a few tens of TeV.

[4] O. Adriani *et al.*, *Phys. Rev. Lett.* **130** (2023) 171002

Fit on the helium spectrum

Helium spectrum is not consistent with a single power law covering the whole range.

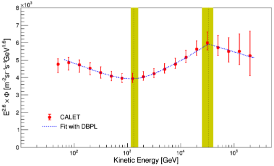

FIGURE 11A: fit with a DBPL function.

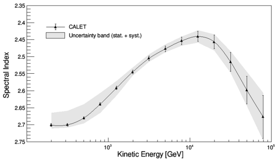

FIGURE 11B: spectral index vs. energy.

DBPL parameter	Fitted value	spectrum region
γ	$-2.703^{+0.005}_{-0.006}(\mathrm{stat})^{+0.032}_{-0.009}(\mathrm{syst})$	low energy
$\Delta\gamma$	$0.25^{+0.02}_{-0.01}(\mathrm{stat})^{+0.02}_{-0.03}(\mathrm{syst})$	hardening
E_0	$1319^{+113}_{-93}(\mathrm{stat})^{+267}_{-124}(\mathrm{syst})$ GeV	hardening
s	$2.7^{+0.6}_{-0.5}(\mathrm{stat})^{+3.0}_{-0.9}(\mathrm{syst})$	hardening
$\Delta\gamma_1$	$-0.22^{+0.07}_{-0.10}(\mathrm{stat})^{+0.03}_{-0.04}(\mathrm{syst})$	softening
E_1	$33.2^{+9.8}_{-6.2}(\mathrm{stat})^{+1.8}_{-2.3}(\mathrm{syst})$ TeV	softening
s_1	~ 30	softening

Spectrum fitted in $60\ \mathrm{GeV} < E < 250\ \mathrm{TeV}$ with a **double broken power law (DBPL)**:

$$\Phi(E) = C\left(\frac{E}{1\ GeV}\right)^{\gamma}\left[1+\left(\frac{E}{E_0}\right)^{s}\right]^{\frac{\Delta\gamma}{s}}\left[1+\left(\frac{E}{E_1}\right)^{s_1}\right]^{\frac{\Delta\gamma_1}{s_1}}$$

The index change $\Delta\gamma$ is proven to be different from zero by more than 8 σ. DBPL fit parameters are consistent, within the errors, with the most recent results of DAMPE.

Comparison of proton and helium spectra

ICHEP 2024

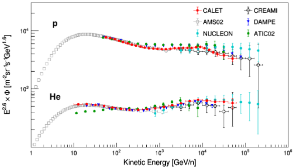

FIGURE 12A: proton and helium spectra vs. energy per nucleon.

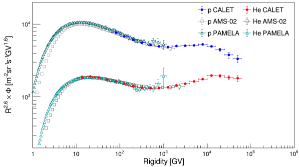

FIGURE 12B: proton and helium spectra vs. rigidity.

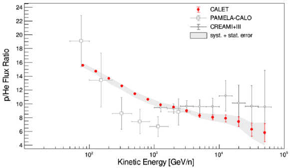

FIGURE 12C: proton to helium ratio vs. energy per nucleon.

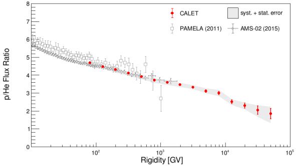

FIGURE 12D: proton to helium ratio vs. rigidity.

- proton and helium spectra harden and soften at around the same region of rigidity;
- the spectral index of helium is harder than that of proton (by ∼0.1) in the whole rigidity range.

The proton and helium spectrum **softening** around 10 TV indicates a possible relation to the energy limit of shock wave acceleration in SNRs.

Boron, carbon and oxygen spectra

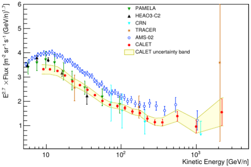

FIGURE 13A: boron spectrum.

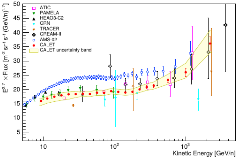

FIGURE 13B: carbon spectrum.

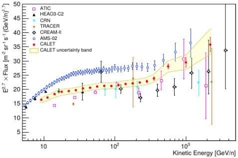

FIGURE 13C: oxygen spectrum.

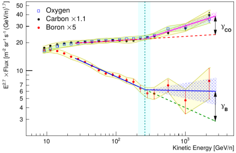

FIGURE 13D: fits with a DPL function.

Spectra measured [5,6] in $8.4\ \mathrm{GeV}/n < E < 3.8\ \mathrm{TeV}/n$. Fit in $25\ \mathrm{GeV}/n < E < 3.8\ \mathrm{TeV}/n$ with a **double power law (DPL)**:

$$\Phi(E) = \begin{cases} C\left(\frac{E}{1\ \mathrm{GeV}}\right)^{\gamma} & E \le E_0 \\ C\left(\frac{E}{1\ \mathrm{GeV}}\right)^{\gamma}\left(\frac{E}{E_0}\right)^{\Delta\gamma} & E > E_0 \end{cases}$$

For carbon and oxygen:

DPL parameter	Fitted value	spectrum region
γ^{CO}	-2.66 ± 0.02	low energy
$\Delta\gamma^{CO}$	0.19 ± 0.04	hardening
E_0^{CO}	$(260 \pm 50)\ \mathrm{GeV}/n$	hardening
χ^2/dof	23/25	-

For boron:

DPL parameter	Fitted value	spectrum region
γ^{B}	-3.03 ± 0.03	low energy
$\Delta\gamma^{B}$	0.32 ± 0.14	hardening
E_0^{B}	$260\ \mathrm{GeV}/n$ (fixed)	hardening
χ^2/dof	5.2/11	-

- C and O fluxes harden in a similar way above 200 GeV/n;
- B spectrum clearly different from C-O as expected for primary and secondary CR.

[5] O. Adriani *et al.*, *Phys. Rev. Lett.* **129** (2022) 251103

[6] P. Maestro *et al.*, *PoS* **(ICRC 2023)** (2024) 058

B/C, B/O and C/O flux ratio

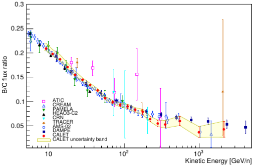

FIGURE 14A: boron to carbon ratio (B/C).

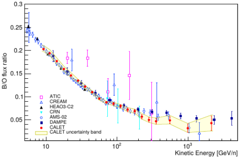

FIGURE 14B: boron to oxygen ratio (B/O).

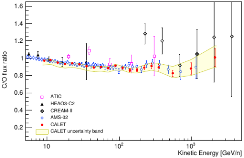

FIGURE 14C: carbon to oxygen ratio (C/O).

We observe that:

- flux ratios of B/C and B/O are in agreement with AMS-02 and lower than DAMPE result above 300 GeV/n, although consistent within the error bars;
- C/O flux ratio as a function of energy is in good agreement with AMS-02;
- at E > 30 GeV/n the C/O ratio is well fitted to a constant value 0.90 ± 0.03, with χ^2/dof = 8.1/13
  - $\Rightarrow$ C and O fluxes have the same energy dependence.
- at E < 30 GeV/n C/O ratio is slightly softer
  - $\Rightarrow$ secondary C from O and heavier nuclei spallation

Iron spectrum and fit

ICHEP 2024

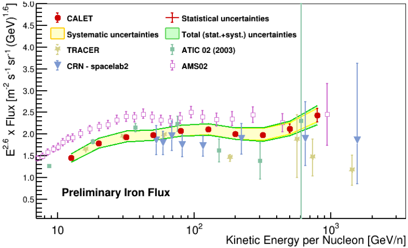

FIGURE 15A: cosmic-ray iron spectrum.

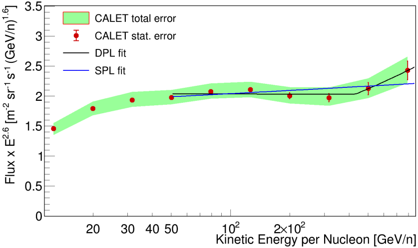

FIGURE 15B: fits with a DPL and a SPL function.

Spectrum measured [7,8] in 10 $\mathrm{GeV}/n < E < 1\ \mathrm{TeV}/n$. Fit in 50 $\mathrm{GeV}/n < E < 1000\ \mathrm{GeV}/n$ with a **DPL** and a **single power law (SPL)**: $\Phi(E) = C\left(\frac{E}{1\ \mathrm{GeV}}\right)^{\gamma}$

DPL parameter	Fitted value	spectrum region
γ	-2.60 ± 0.01 (stat) ± 0.08 (syst)	low energy
$\Delta\gamma$	0.29 ± 0.27	hardening
E_0	428 ± 314 GeV/n (fixed)	hardening
χ^2/dof	0.8/3	-
SPL parameter	**Fitted value**	**spectrum region**
γ	-2.56 ± 0.01 (stat) ± 0.03 (syst)	all energy
χ^2/dof	2.7/5	-

We observe that:

- the spectrum is consistent with CRN and ATIC
- the significance of the fit with the DPL is not sufficient to exclude the possibility of a SPL.

[7] O. Adriani *et al.*, *Phys. Rev. Lett.* **126** (2021) 241101
[8] F. Stolzi *et al.*, *PoS* **(ICRC 2023)** (2024) 061

Nickel spectrum and fit

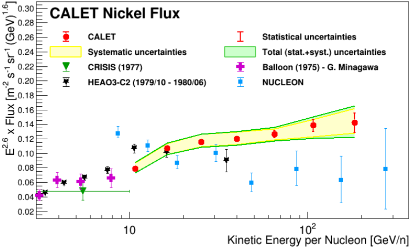

FIGURE 16A: cosmic-ray nickel spectrum.

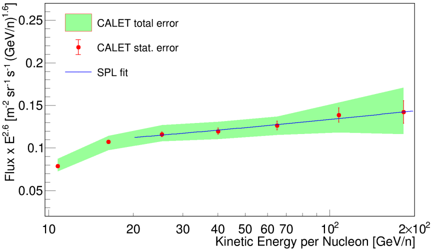

FIGURE 16B: fit with a SPL function.

Spectrum measured [8,9] in $8.8\ \mathrm{GeV}/n < E < 240\ \mathrm{GeV}/n$. Fit: $20\ \mathrm{GeV}/n < E < 240\ \mathrm{GeV}/n$ with a **SPL**: $\gamma = -2.49 \pm 0.03$ (stat) ± 0.07 (syst) (χ^2/dof = 0.1/3)

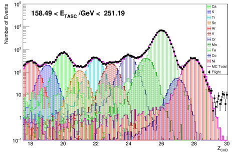

FIGURE 16C: charge distributions.

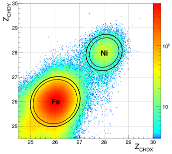

FIGURE 16D: Fe-Ni charge separation.

- Slightly softer than NUCLEON results
- SPL well consistent with CALET data

[9] O. Adriani *et al.*, *Phys. Rev. Lett.* **128** (2022) 131103

Ultra heavy nuclei ($26 < Z \leq 44$)

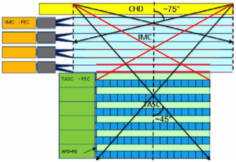

FIGURE 17A: acceptance for UH trigger.

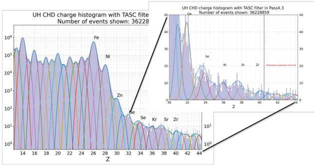

FIGURE 17B: UH CHD charge histogram with TASC filter.

- the Ultra Heavy (UH) trigger uses CHD and IMC (first 4 layers) to quadruple the geometric factor GF $\sim$ 4400 cm^2 sr without energy information ($\sim$260 million events);
- a data subset cross the top of the TASC with energy information ($\sim$65 million events).

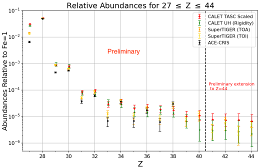

FIGURE 17C: UH abundances for $Z > 26$.

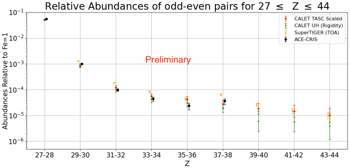

FIGURE 17D: relative abundances of the Odd-Even pairs.

The CALET UH element ratios relative to Fe are consistent with SuperTIGER and ACE-CRIS abundances [10].

[10] V. Zober *et al.*, *PoS* **(ICRC 2023)** (2024) 088

γ-rays and gravitational waves

- Observations with High Energy (HE) trigger are always active (E > ~10 GeV);
- observations with Low Energy γ (LE-γ) trigger are active at low geomagnetic latitudes (E > ~1 GeV);
- trigger of CGBM instrument prompts CALET to temporarily activate LE-γ mode to search for transient counterparts;
- transient analysis pipeline allows for quick follow-up of GRBs or LIGO/Virgo GW triggers;
- observations corresponding to triggers in LIGO/Virgo O3-O4 run were analyzed.

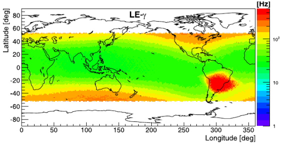

Figure 18a: LE-γ trigger rate [11].

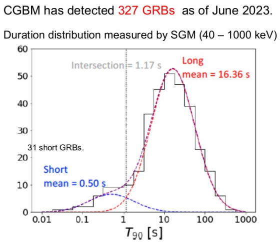

Figure 18b: duration distribution measured by SGM.

No candidate of EM counterparts was found in CALET data. We obtained upper limits of high energy γ-ray flux [12].

[11] Y. Asaoka *et al.*, *Astr. Phy.* **100** (2018) 29

[12] O. Adriani *et al.*, *Astr. Jou.* **933** (2022) 85

γ-ray sky map and energy spectra

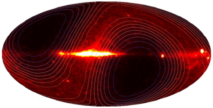

Figure 19a: skymap for LE-γ triggers.

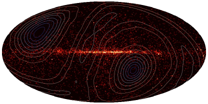

Figure 19b: skymap for HE triggers.

- Effective area: ~400 cm^2
- Angular resolution: < 0.2° (> 10 GeV)
- Energy resolution: 2% (> 10 GeV)

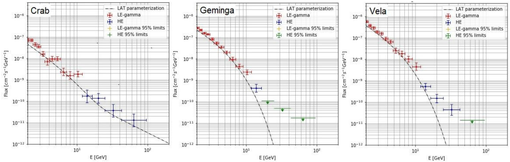

Figure 19c: energy spectra of some point sources (Crab, Geminga, Vela).

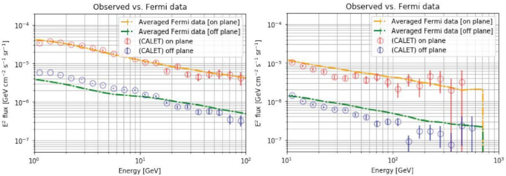

Figure 19d: Galactic and off-Galactic plane spectra for LE-γ (left) and HE (right) data.

The spectra for point sources and diffuse components are found to be consistent with those obtained by Fermi-LAT [13].

[13] M. Mori *et al.*, *PoS* **(ICRC 2023)** (2024) 708

Solar modulation and drift model

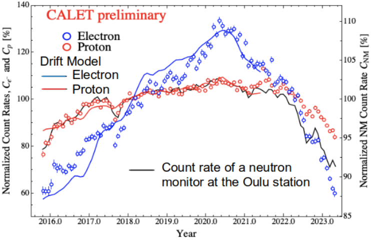

FIGURE 20A: time profiles of the normalized count rates of electrons C_{e-}, protons C_p and neutron monitor C_{NM}.

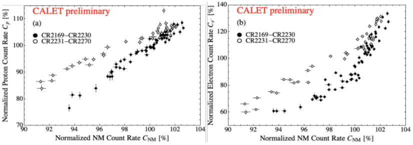

FIGURE 20B: proton and electron count rates at the average rigidity of 3.8 GV as a function of neutron monitor count rates at the Oulu station during the descending phase in the 24th solar cycle (closed circles) and the ascending phase in the 25th solar cycle (open circles).

- We have observed a clear charge-sign dependence of the solar modulation of GCRs, showing that variation amplitude of C_{e-} is much larger than that of C_p at the same average rigidity [14,15].
- We also have succeeded in reproducing variations of C_{e-} and C_p simultaneously with a numerical drift model of the solar modulation, which implies that the drift effect plays a major role in the long-term modulation of GCRs.
- We also find a clear difference between ratios, C_p/C_{NM} , during the descending phase of the 24th solar cycle and the ascending phase of the 25th solar cycle.

[14] O. Adriani *et al.*, *Phys. Rev. Lett.* **130** (2023) 211001 [15] S. Miyake *et al.*, *PoS* **(ICRC 2023)** (2024) 1253

Conclusions

CALET was successfully launched on August 19th, 2015, and is successfully carrying out observations since October 2015 with stable instrument performance

- Main results discussed in this presentation:
  - all-electron up to 7.5 TeV, cut-off confirmed and hint of SNR contribution [PRL 131, 191001 (2023)];
  - proton up to 60 TeV, hardening and softening confirmed [PRL 129, 101102 (2022)];
  - helium up to 250 TeV, hardening confirmed and onset of a softening [PRL 130, 171002 (2023)];
  - carbon and oxygen up to 3.8 TeV/*n*, hardening clearly observed [PRL 125, 251102 (2020) and ICRC2023];
  - boron up to 3.8 TeV/*n*, harden more than C-O [PRL 129, 251103 (2022) and ICRC2023];
  - iron up to 1 TeV/*n*, hint of hardening [PRL 126, 241101 (2021) and ICRC2023];
  - nickel up to 240 GeV/*n*, more accurate high energy measurement [PRL 128, 131103 (2022) and ICRC2023];
  - ultra heavy nuclei: large acceptance analysis, consistent with SuperTIGER [ICRC2023];
  - transient low energy gamma and X-rays: no candidate of EM counterparts [ApJ 933:85, ApJL 829:L20];
  - high energy gamma-rays: diffuse flux, source spectra [ICRC2023];
  - solar modulation: charge-sign dependence [PRL 130, 211001 (2023) and ICRC2023].
- Other important topics were not discussed in this presentation, e.g. space weather, nuclei ratios, *etc.*

Extended operations recently approved by JAXA/NASA/ASI through the end of 2030.

Thank you

for your attention

We gratefully acknowledge JAXA's contributions to the development of CALET and to the operations onboard the International Space Station. The CALET effort in Italy is supported by ASI under Agreement No. 2013- 018-R.0 and its amendments. The CALET effort in the United States is supported by NASA through Grants No. 80NSSC20K0397, No. 80NSSC20K0399, and No. NNH18ZDA001N-APRA18-0004. This work is supported in part by JSPS Grant-in- Aid for Scientific Research (S) Grant No. 19H05608 in Japan.

Backup slides

CALET full authors list

O. Adriani,[1,2] Y. Akaike,[3,4] K. Asano,[5] Y. Asaoka,[5] E. Berti,[2,6] G. Bigongiari,[7,8] W. R. Binns,[9] M. Bongi,[1,2] P. Brogi,[7,8] A. Bruno,[10] N. Cannady,[11,12,13] G. Castellini,[6] C. Checchia,[7,8] M. L. Cherry,[14] G. Collazuol,[15,16] G. A. de Nolfo,[10] K. Ebisawa,[17] A. W. Ficklin,[14] H. Fuke,[17] S. Gonzi,[1,2,6] T. G. Guzik,[14] T. Hams,[11] K. Hibino,[18] M. Ichimura,[19] W. Ishizaki,[5] M. H. Israel,[9] K. Kasahara,[20] J. Kataoka,[21] R. Kataoka,[22] Y. Katayose,[23] C. Kato,[24] N. Kawanaka,[25,26] Y. Kawakubo,[14] K. Kobayashi,[3,4] K. Kohri,[26,27] H. S. Krawczynski,[9] J. F. Krizmanic,[12] P. Maestro,[7,8] P. S. Marrocchesi,[7,8] A. M. Messineo,[8,28] J. W. Mitchell,[12] S. Miyake,[29] A. A. Moiseev,[12,13,30] M. Mori,[31] N. Mori,[2] H. M. Motz,[32] K. Munakata,[24] S. Nakahira,[17] J. Nishimura,[17] M. Negro,[14] S. Okuno,[18] J. F. Ormes,[33] S. Ozawa,[34] L. Pacini,[2,6] P. Papini,[2] B. F. Rauch,[9] S. B. Ricciarini,[2,6] K. Sakai,[11,12,13] T. Sakamoto,[35] M. Sasaki,[12,13,30] Y. Shimizu,[18] A. Shiomi,[36] P. Spillantini,[1] F. Stolzi,[7,8] S. Sugita,[35] A. Sulaj,[7,8] M. Takita,[5] T. Tamura,[18] T. Terasawa,[5] S. Torii,[3] Y. Tsunesada,[37,38] Y. Uchihori,[39] E. Vannuccini,[2] J. P. Wefel,[14] K. Yamaoka,[40] S. Yanagita,[41] A. Yoshida,[35] K. Yoshida,[20] and W. V. Zober[9]

[1] *University of Florence, Italy*
[2] *INFN, Florence Division, Italy*
[3] *WISE, Waseda University, Japan*
[4] *JEM Utilization Center, JAXA, Japan*
[5] *ICRR, University of Tokyo, Japan*
[6] *IFAC, CNR, Italy*
[7] *University of Siena, Italy*
[8] *INFN, Pisa Division, Italy*
[9] *Washington University, St. Louis, USA*
[10] *Heliospheric Physics Laboratory, NASA/GSFC, USA*
[11] *CSST, University of Maryland, Baltimore County, USA*
[12] *Astroparticle Physics Laboratory, NASA/GSFC, USA*
[13] *CRESST, NASA/GSFC, USA*
[14] *Louisiana State University, USA*
[15] *University of Padova, Italy*
[16] *INFN, Padova Division, Italy*
[17] *ISAS, JAXA, Japan*
[18] *Kanagawa University, Japan*
[19] *Hirosaki University, Japan*
[20] *Shibaura Institute of Technology, Japan*
[21] *ASE, Waseda University, Japan*
[22] *NIPR, Japan;*
[23] *Yokohama National University, Japan*
[24] *Shinshu University, Japan*
[25] *Tokyo Metropolitan University, Japan*
[26] *NAOJ, Japan*
[27] *IPNS, Japan*
[28] *University of Pisa, Italy*
[29] *NIT (KOSEN), Ibaraki College, Japan*
[30] *University of Maryland, College Park, USA*
[31] *Ritsumeikan University, Japan*
[32] *Waseda University, Japan*
[33] *University of Denver, USA*
[34] *NICT, Japan*
[35] *Aoyama Gakuin University, Japan*
[36] *Nihon University, Japan*
[37] *Osaka Metropolitan University, Japan*
[38] *NITEP, Osaka Metropolitan University, Japan*
[39] *QST, Japan*
[40] *Nagoya University, Japan*
[41] *Ibaraki University, Japan*

PI: Japan
Co-PI: Italy
Co-PI: USA

CALET objectives

The technical characteristics of the instrument enable the CALET mission to address the main outstanding questions of high-energy cosmic ray physics.

Scientific objectives	**Observation target**	**Energy range**
Nearby CR sources	Electron Spectrum	100 GeV - 20 TeV
Dark Matter	Signatures in e/γ spectra	100 GeV - 20 TeV
CR origin & acceleration	Electron spectrum p-Fe individual spectra Ultra heavy ions ($28 < Z \leq 40$)	1 GeV - 20 TeV 10 GeV - 10^3 TeV a few GeV/n
Galactic CR propagation	B/C sub-Fe/Fe ratios	up to some TeV/n
Solar physics	Electron flux	< 10 GeV
Transient phenomena	γ-rays & X-rays	7 keV - 20 MeV

CALET main features:

- wide dynamic range (1-10^6 MIP);
- large thickness (30 X_0, 1.3 λ_I);
- excellent charge ID (0.2 e^-)

CALET can cover the whole energy range previously investigated in separate subranges by **magnetic spectrometers** and **calorimeters**.

The CALET instrumentation

Overview of the main detector (CAL) instrumentation:

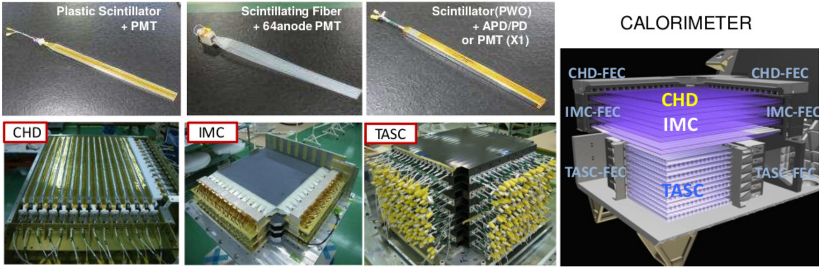

FIGURE 21: overview of the CALET main detector (CAL) instrumentation.

	CHD (CHarge Detector)	IMC (IMaging Calorimeter)	TASC (Total AbSorption Calorimeter)
Measure	Charge (Z=1-40)	Tracking, Particle ID	Energy, e/p Separation
Geometry (Material)	Plastic Scintillator 14 paddles $\times$ 2 layers (X,Y): 28 paddles Paddle Size: $(32 \times 10 \times 450)$ mm^3	448 SciFi $\times$ 16 layers (X,Y) : 7168 SciFi 7 W layers (3 X_0): $0.2 \cdot X_0 \times 5 + 1 \cdot X_0 \times 2$ SciFi size : $(1 \times 1 \times 448)$ mm^3	16 PWO logs $\times$ 12 layers (X,Y): 192 logs log size: $(19 \times 20 \times 326)$ mm^3 Total Thickness: 27 X_0, ~ 1.2 λ_I
Readout	PMT + CSA	64-anode PMT + ASIC	APD/PD + CSA PMT + CSA (for Trigger) @ top layer

The total thickness of the instrument is equivalent to **30 X_0** and **1.3 λ_I**.

Examples of CALET event candidates

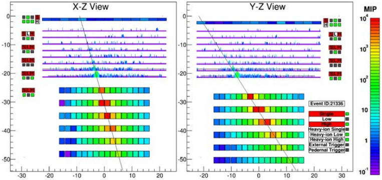

FIGURE 22A: electron (or positron), E = 3.05 TeV.

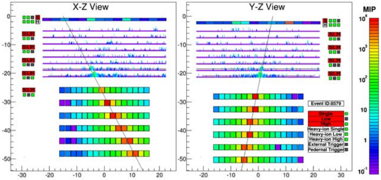

FIGURE 22B: proton, E_{TASC} = 2.89 TeV (same as electron).

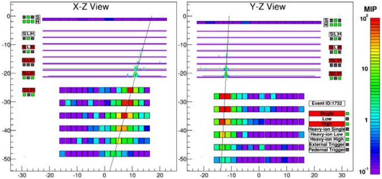

FIGURE 22C: γ-ray, E = 44.3 GeV.

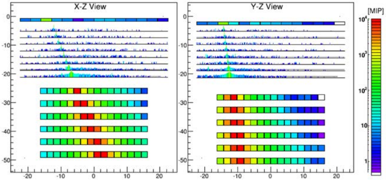

FIGURE 22D: iron, E_{TASC} = 9.03 TeV.

CALET capability of particle identification:

- the calorimeter absorbs the full electron shower energy even in the TeV range;
- charge measurement (CHD and IMC) identifiy elements from Z = 1 to 26 and above;
- γ-rays are identified as charge zero (no signal before the pair creation).

Detector performance

- CHD charge resolution: from 0.15 *e* (B and C) to 0.35 *e* (Fe);
- angular resolution:
  - $\sim 0.1^\circ$ for *e*, *p*, nuclei;
  - $\sim 0.2^\circ$ for γ-ray (E > 50 GeV);
- energy resolution:
  - $\sim 2\%$ (E > 10 GeV) for *e* and γ-ray;
  - $\sim 30 - 35\%$ for *p*, nuclei;
- e/p separation: $\sim 10^{-5}$. The proton contamination is less than 10% up to 7.5 TeV
- Charge identification:
  - for *p*, He and light nuclei is achieved by CHD + IMC;
  - for heavy nuclei is achieved by CHD (signal saturation in the IMC layers).

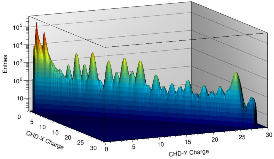

FIGURE 23A: charge distribution from proton to Nickel (CHD).

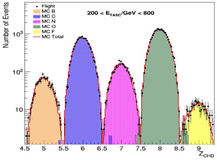

FIGURE 23B: charge distribution for low Z (CHD).

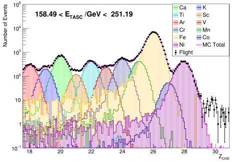

FIGURE 23C: charge distribution for high Z (CHD).

Energy measurement: a wide dynamic range 1-10^6 MIPs

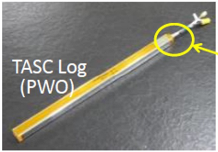

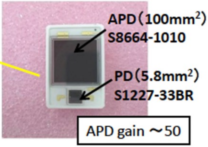

"MIP" peak in PWO: Obs. vs. MC

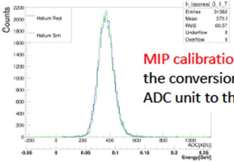

MIP calibration determines the conversion factor from ADC unit to the energy

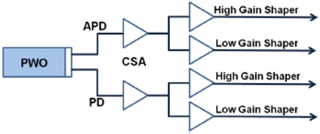

The whole dynamic range was calibrated by UV laser irradiation on ground :

1) The linearity of each gain range is confirmed in the range of 1.4-2.5 %.
2) Each channel covers from 1 MIP to 10^6 MIPs.

APD-H	APD-L	PD-H	PD-L
1.4%	1.5%	2.5%	2.2%

The correlation between adjacent gain ranges is calibrated by using in-flight data in each channel.

APD-H / APD-L	APD-L / PD-H	PD-H / PD-L
0.1%	0.7%	0.1%

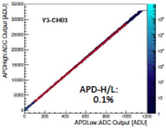

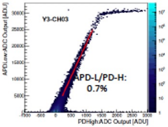

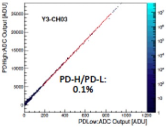

Example of energy distribution in one PWO log

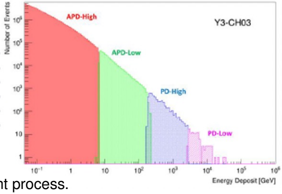

FIGURE 24: overview of the energy measurement process.

Nuclei measurement: charge identification with CHD and IMC

Single element identification for p, He and light nuclei due to CHD+IMC charge analysis.

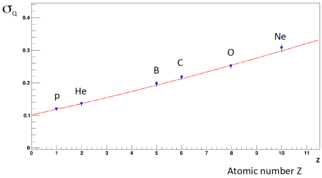

FIGURE 25A: IMC charge resolution (multiple dE/dx sampling in scintillating fibers). Charge separation in B to C: $\sim 5\sigma$.

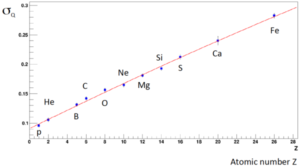

FIGURE 25B: CHD charge resolution (2 layers combined). Charge separation in B to C: $\sim 7\sigma$.

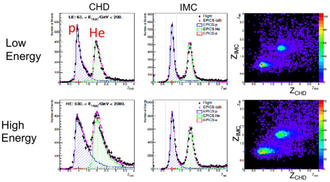

FIGURE 25C: charge identification with CHD and IMC.

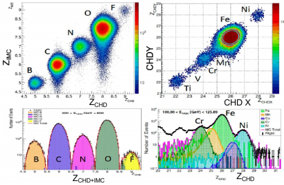

FIGURE 25D: charge identification vs. Z.

Deviation from Z^2 response is corrected both in CHD and IMC using a core + halo ionization model (Voltz).

Energy measurement: energy scale and resolution

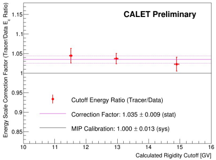

FIGURE 26A: absolute energy scale calibration (electrons).

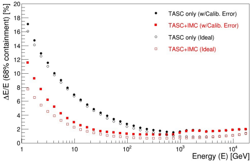

FIGURE 26B: simulated energy resolution (electrons).

Electrons:

- absolute energy scale calibration for electrons using rigidity cutoff + beam calibration at CERN-SPS;
- simulated energy dependence of electron energy resolution: < 2% above 20 GeV using both TASC and IMC including the calibration errors.

Hadrons:

Beam calibration (CERN-SPS in 2015) with ion fragments at 13, 19 and 150 GeV/n:

- linearity assessed up to ~ 6 TeV with primary beam of ^{40}Ar at 150 GeV/n;
- fraction of particle energy released in TASC is ~ 20%;
- energy resolution: ~ 30-35%.

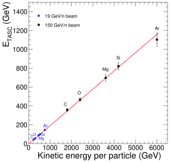

FIGURE 26C: linearity in energy (hadrons).

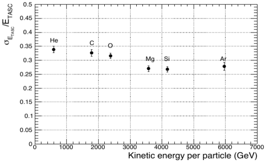

FIGURE 26D: energy resolution (hadrons).

Spectral Fit of B/C and B/O

B/C and B/O ratio fitted to a DPL and to functions from a leaky-box model describing the particle transport in the Galaxy.

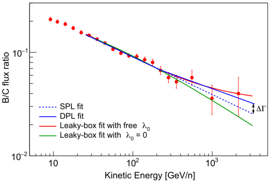

FIGURE 27A: fits with a SPL and a DPL function.

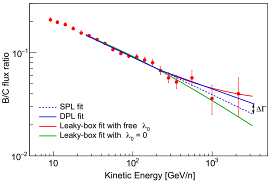

FIGURE 27B: Leaky-Box model (λ_0 fixed or free).

Simultaneous fit to B/C and B/O (E > 25 GeV/n) with same parameters except normalization:

- SPL fit: Γ = -0.376 ± 0.014 (χ^2/dof = 19/27)
- DPL fit: $\Delta\Gamma$ = 0.22 ± 0.10 (χ^2/dof = 15/26)

Leaky-Box (LB) model:

$$\frac{\Phi_B(E)}{\Phi_C(E)} = \frac{\lambda(E)\,\lambda_B}{\lambda(E)+\lambda_B}\left[\frac{1}{\lambda_{C\to B}} + \frac{\Phi_O(E)}{\Phi_C(E)}\frac{1}{\lambda_{O\to B}}\right]$$

$$\frac{\Phi_B(E)}{\Phi_O(E)} = \frac{\lambda(E)\,\lambda_B}{\lambda(E)+\lambda_B}\left[\frac{1}{\lambda_{O\to B}} + \frac{\Phi_O(E)}{\Phi_C(E)}\frac{1}{\lambda_{C\to B}}\right]$$

$$\lambda(E) = kE^{-\delta} + \lambda_0$$

λ_B: interaction length of B nuclei with matter of the ISM;
$\lambda_{C\to B}(\lambda_{O\to B})$: average path length for a nucleus C (O) to spall into B;
$\lambda(E)$: mean escape path length;
δ: diffusion coefficient spectral index;
λ_0: residual path length (interpreted as source grammage).

LB parameter	$\lambda_0 = 0$ fixed	λ_0 free
k	(13.1 ± 0.2) g/cm^2	(13.0 ± 0.3) g/cm^2
δ	0.61 ± 0.01	0.81 ± 0.04
λ_0	0 g/cm^2	(1.17 ± 0.16) g/cm^2
χ^2/dof	58.3/38	17.9/37

Significance of $\lambda_0 \neq 0 > 5\sigma$. Residual path length could explain the flattening of B/C, B/O ratios at high energies.

CALET Gamma-ray Bursts Monitor (CGBM)

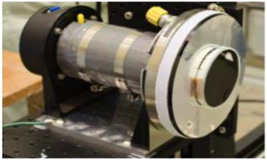

Figure 28a: Hard X-ray Monitor (HXM).

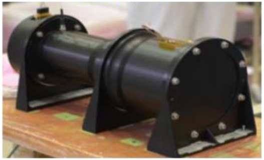

Figure 28b: Soft Gamma-ray Monitor (SGM).

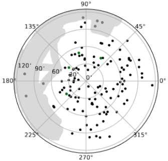

Figure 28c: SGM field-of-view.

The Calet Gamma-ray Burst Monitor (CGBM):

- consists of two Hard X-ray Monitor (HXM) and one Soft Gamma-ray Monitor (SGM);
  - HXM: $LaBr_3$ scintillator (energy range: 7 keV $\sim$ 1 MeV);
  - SGM: BGO scintillator (energy range: 100 keV $\sim$ 20 MeV);
- collects light curve data and spectral data for each 1/8 s and 4 s, respectively.
- if CGBM detects a transient, CGBM captures event data (62.5 μs, 4096 x 2 energy channels).

CGBM can detect short GRBs, primary candidates for the counterparts of gravitational wave sources.